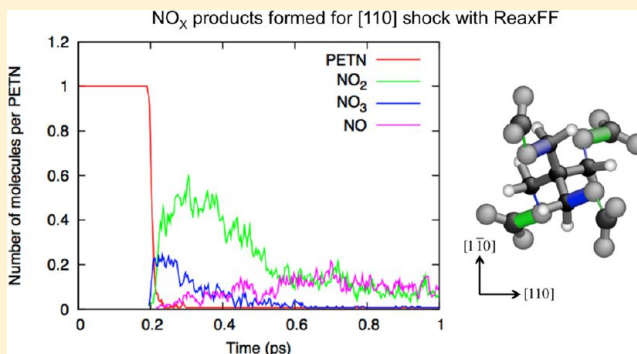


Atomistic Simulation of Orientation Dependence in Shock-Induced Initiation of Pentaerythritol Tetranitrate

Tzu-Ray Shan,* Ryan R. Wixom, Ann E. Mattsson, and Aidan P. Thompson

Sandia National Laboratories, Albuquerque, New Mexico 87185, United States

ABSTRACT: The dependence of the reaction initiation mechanism of pentaerythritol tetranitrate (PETN) on shock orientation and shock strength is investigated with molecular dynamics simulations using a reactive force field and the multiscale shock technique. In the simulations, a single crystal of PETN is shocked along the [110], [001], and [100] orientations with shock velocities in the range 3–10 km/s. Reactions occur with shock velocities of 6 km/s or stronger, and reactions initiate through the dissociation of nitro and nitrate groups from the PETN molecules. The most sensitive orientation is [110], while [100] is the most insensitive. For the [001] orientation, PETN decomposition via nitro group dissociation is the dominant reaction initiation mechanism, while for the [110] and [100] orientations the decomposition is via mixed nitro and nitrate group dissociation. For shock along the [001] orientation, we find that CO–NO₂ bonds initially acquire more kinetic energy, facilitating nitro dissociation. For the other two orientations, C–ONO₂ bonds acquire more kinetic energy, facilitating nitrate group dissociation.



1. INTRODUCTION

Understanding the physics and chemistry of detonation in energetic materials, such as pentaerythritol tetranitrate (PETN), is important not only in military applications but also in civil engineering (mining and excavation) and in many specialized applications such as emergency passenger restraint systems and rocket propulsion. For many materials, the detonation velocity and shockwave amplitude of an established steady-state detonation front can be reliably estimated from simple stoichiometric and thermochemical considerations. In contrast, the processes by which detonation is initiated in the unreacted material are complex and difficult to predict. Sensitivity is a measure of how small a perturbation is required to initiate detonation, and experimentally it has been observed that for PETN sensitivity is dependent upon the crystallographic orientation of the shockwave propagation direction in the energetic material.¹

Shock initiation sensitivity of PETN crystals along different orientations has been related to the degree of steric hindrance occurring in the slip systems stimulated by uniaxial compression.^{1–3} For sensitive orientations such as [110] and [001], the stimulated slip systems are strongly hindered. Layers of molecules in adjacent planes interpenetrate each other, preventing them from easily sliding past each other. This steric hindrance allows shear stresses to become quite large before plastic yielding occurs, resulting in a proportionately large amount of work energy that is rapidly deposited in localized regions when yielding finally occurs. These regions experience a large increase in local temperature that allows initiation to occur. In contrast, the slip systems stimulated by uniaxial compression in insensitive orientations such as [100] and [101]

do not exhibit steric hindrance. Adjacent layers of molecules do not interpenetrate and the slip systems cannot sustain large shear stresses. As a result, far less plastic work is deposited, and the temperature rise due to plastic deformation is less.

Compression shear MD simulations of PETN crystals along the [110] and [001] orientations support the experimental notion that orientation-dependent shock sensitivity is controlled by steric hindrance in slip planes.⁴ Large-scale nonequilibrium molecular dynamics (NEMD) simulations with the ReaxFF reactive force field showed effects of endothermic and exothermic reactions on PETN shock velocity.⁵

Several studies have used ab initio quantum electronic structure methods to understand the reaction initiation mechanism of PETN. A quantum mechanical molecular dynamics study using a semiempirical method under the Hartree–Fock formalism of collisions of two PETN molecules along the [110], [001], and [100] orientations indicated that the dissociation of the nitro bond (CO–NO₂) is the primary initiation reaction, independent of collision orientation.⁶ A combined experimental and computational work utilizing time-resolved emission spectroscopy and a post-Hartree–Fock method on PETN crystals shocked along [110] and [100] orientations proposed a four-step chemical initiation mechanism.⁷ In that work, PETN molecule dissociation during shock initiation was proposed to start with splitting of the nitrate bond (C–ONO₂) yielding a carbocation and a nitrate ion (NO₃[–]).

Received: October 22, 2012

Revised: December 20, 2012

Published: December 31, 2012



Table 1. Dissociation Barriers (in kJ/mol) of a Gas-Phase PETN Molecule

reaction channel	PM3 ⁶	DFT ⁶	ReaxFF
PETN \rightarrow NO ₂ + C ₅ H ₈ O ₁₀ N ₃ (I)	64.5	157.8	143.6
PETN \rightarrow NO ₂ + CH ₂ O + C ₄ H ₆ O ₉ N ₃ (II)	142.4	–	165.0
PETN \rightarrow NO ₂ + H + C ₅ H ₇ O ₁₀ N ₃ (III)	174.6	264.2	179.5
PETN \rightarrow NO ₃ + C ₅ H ₈ O ₉ N ₃ (IV)	280.5	305.6	209.8
PETN \rightarrow O + C ₅ H ₈ O ₁₁ N ₄ (V)	356.7	355.5	314.3

The subsequent observed reactions were the exothermic dissociation of the nitrate ion into an oxygen ion (O²⁻) and a nitro ion (NO₂⁺), and the rebinding of oxygen ion to the carbocation.

Both of these studies were performed using either colliding pairs of molecules or very small bulk PETN simulation cells, and hence presented a somewhat idealized representation of shock compression. The goal of the current work is to perform simulations on a scale capable of capturing the different local deformation mechanisms that occur when PETN is compressed along different crystal orientations, while still providing a quantitatively accurate description of chemical reaction dynamics. In particular, we wish to examine whether the preferred initiation pathway is affected by shock orientation. To do this, we perform simulations of shock compression along the [110], [001], and [100] orientations, for a 4 × 4 × 4 supercell of PETN containing several thousand atoms, using the ReaxFF potential. In the following section we describe the computational details, including ab initio calculations, ReaxFF force field, and shock simulations. In section 3 we present the comparison of ReaxFF with ab initio and experimental results, and the results and discussions of shock simulations, including a detailed analysis of the chemical pathways occurring for shocks in the [110], [001], and [100] directions.

2. THEORETICAL METHODS

2.1. Density Functional Theory Calculations. Density functional theory based molecular dynamics (DFT-MD) simulations were previously used to determine the unreacted principle Hugoniot of PETN. The computational details and preliminary results have been published elsewhere,⁸ but the details of the technique follow, and section 3.2 describes how the calculations were used to obtain the unreacted Hugoniot. DFT-MD has been shown to provide extremely accurate predictions of the unreacted Hugoniot for a wide variety of materials.^{9,10} The calculations, utilizing the AM05 functional,¹¹ were performed with the Vienna ab initio simulation package (VASP 5.2),^{12–14} using strictly converged settings.¹⁵ The plane-wave cutoff was set to 800 eV and *k*-point sampling with mean-value point (1/4,1/4,1/4) was used. The ionic time step was set to 0.4 fs. The reference state was taken to be the experimental structure and volume for PETN (tetragonal space group P4̄₂1c, *a*₀ = 0.93 776, *c*₀ = 0.67 075 nm).¹⁶

2.2. Molecular Dynamics with Reactive Force Field. The reactive and variable charge empirical force field, ReaxFF, is used in this work. ReaxFF includes many-body and nonbonded interactions (Lennard-Jones and Coulombic electrostatics) with no predefined bonds and angles,^{17,18} and was applied to study shock waves in high-energy materials¹⁹ for the first time. Bond order terms allow the formation of new bonds as well as the dissociation of existing bonds due to reactions, and are used to determine the strength of chemical

bonds. We use the same parametrization as in the work of Budzien et al.,⁵ which was developed by Strachan et al.^{19,20} However, in the work of Budzien et al.⁵ chemical bonds and molecular species were determined based on instantaneous bond order values of the specific sampled snapshots in a postprocessing fashion. If the system is highly reactive and molecular bonds are forming and breaking more frequently than the sampling interval, this could produce an incomplete description of the bonding information and molecular species analysis. In addition, instantaneous snapshots of atoms undergoing high-temperature dynamics inevitably contain pairs of atoms that are undergoing a brief collision that is mistaken for a bonded state. Conversely, pairs of bonded atoms may be undergoing a large-amplitude vibration that is mistaken for a nonbonded state. To eliminate these difficulties, we have added a capability for identifying bonds and chemical species at frequent intervals during the simulation run (on-the-fly) based on time-averaged bond order values. In this work, bond order values are sampled every 0.25 fs and every 10 samples are used to calculate averaged bond order values for the on-the-fly determination of chemical bonds and molecular species. This allows us to efficiently output an inventory of molecular species every 2.5 fs.

2.3. Shock Simulations with Multiscale Shock Technique. Shock simulations in this work are performed using the multiscale shock technique (MSST), which is a method specifically formulated for studying shocked materials by Reed et al.²¹ Conservation of mass, momentum, and energy is invoked to drive the volume and temperature of the atomistic simulation system to a Hugoniot state, consistent with a material undergoing steady-state shock compression with shock velocity *U*_s with respect to the frame of the uncompressed material. To simulate a shock with MD using MSST, a desired value of *U*_s is specified. The resultant dynamic equations obtained from the extended Lagrangian are then integrated forward in time, taking the system to the desired final pressure via uniaxial compression along a predefined shock orientation. Properties such as temperature, stress, and the velocity of the material with respect to the frame of the uncompressed material (i.e., particle velocity *U*_p) can be obtained. MSST has been successfully applied to the studies of shocked nitromethane,^{22,23} graphite, diamond,²⁴ and other energetic materials.²⁵ The primary reason for choosing MSST over explicit NEMD simulation of shockwave propagation is computational cost. In NEMD, the length of the simulation cell must be sufficient to fully contain the shockwave over the duration of the simulation, and hence the required number of atoms increases linearly with the shock speed and also the duration of the simulation. It has been shown²⁶ that MSST can reproduce the final compressed states observed in NEMD simulations. Both ReaxFF and MSST are implemented in the large-scale atomic/molecular massively parallel simulator (LAMMPS) software package,^{27,28} with which all MD simulations in this work are carried out.

3. RESULTS AND DISCUSSION

3.1. Dissociation Barrier of a Gas-Phase PETN Molecule. To examine the accuracy of ReaxFF in describing the dissociation behavior of a gas-phase PETN molecule, we calculate the dissociation barriers along several channels with ReaxFF utilizing the nudged elastic band (NEB) technique.^{29,30} The results are compared to ab initio calculations of PM3 and DFT performed by Wu et al.⁶ presented in Table 1. The dissociation barriers are qualitatively and quantitatively predicted by the ReaxFF potential: the dissociation of the CO–NO₂ bond is most favored, while the dissociation of C–ONO₂ and CON–O bonds are least energetically favorable.

3.2. Hugoniot Plots from Isotropic Compressions. The fidelity of the ReaxFF potential to reproduce and predict the properties of PETN single crystals under high compressions is verified by comparing the Hugoniot plots to DFT-MD simulations and experimental data compiled by Marsh.³¹ PETN single crystals with density 1.774 g/cm³, comparable to the experimental value, are used as equilibrium volume, V_0 , for DFT-MD and ReaxFF-MD simulations. DFT data are calculated using one PETN unit cell, while ReaxFF calculations used a supercell of $4 \times 4 \times 4$ unit cells (Figure 1). Experimental

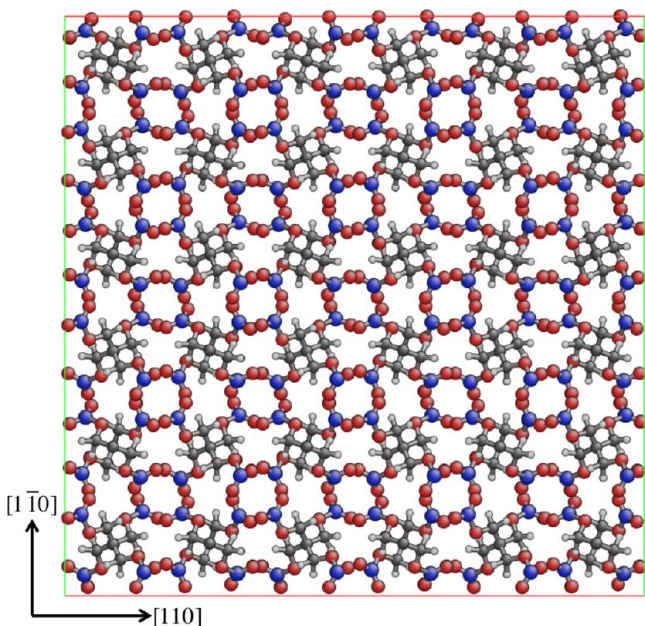


Figure 1. Ball-and-stick model of a $4 \times 4 \times 4$ PETN supercell viewing the (001) plane; all ReaxFF-MD MSST shock simulations in this work are performed with periodic PETN single-crystal cells of this size. Large red atoms are oxygen, large blue atoms are nitrogen, medium gray atoms are carbon, and small white atoms are hydrogen.

data were obtained with uniaxially compressed, single crystals. Points along the Hugoniot are found by setting the volume ($V < V_0$) and equilibrating by running an NVT simulation at ambient temperature (Nosé–Hoover thermostat, $T = 300$ K) for up to 6 and 10 ps for DFT- and ReaxFF-MD simulations, respectively. The temperature of the cell is then instantly increased to a higher temperature and the NVT simulations are continued for an additional 6 and 10 ps for DFT and ReaxFF at that higher temperature. At each compression, three or more high-temperature simulations are performed. We choose to approximate the real shock experiment results with isotropic compression rather than hydrostatic pressure, since we could

not apply a specified stress loading and so could not apply hydrostatic pressure.

The pressure and energy from equilibrated portions of the high-temperature simulations are then used to write equations for energy $U(T)$ and pressure $P(T)$. These equations, and the conservation of energy Rankine–Hugoniot relation

$$U(T) - U_0 = [P(T) + P_0][V_0 - V]/2$$

are used to solve for the temperature on the Hugoniot. That temperature is then used to determine the pressure and energy on the Hugoniot for that volume. Care was taken to ensure that the chosen simulation temperatures bracket the predicted Hugoniot temperature, and it is verified that no chemical reactions occurred during the course of simulations. Repeating this procedure, with increasing densities, allows one to map out the unreacted Hugoniot to very high pressures, much higher than is achievable experimentally. Illustrated in Figure 2 are comparisons of the (a) pressure–volume, (b) shock velocity–particle velocity, and (c) temperature–pressure Hugoniot plots from DFT-MD and ReaxFF-MD simulations to the experimental data. Although ReaxFF shows a larger deviation from DFT and experimental data at higher compressions and pressures, the Hugoniot plots indicate that ReaxFF is able to describe PETN under extreme conditions.

3.3. Shock Velocity–Particle Velocity Hugoniots from MSST Shock Simulations. Comparison of the shock velocity–particle velocity ($U_s - U_p$) Hugoniot from MSST shock simulations of this work with the experimental data of Marsh^{31,32} and Dick³ is illustrated in Figure 3. The Marsh and Dick data were obtained with PETN single crystals of densities around 1.77 g/cm³, while the MSST shock simulations are performed with $4 \times 4 \times 4$ PETN supercells of densities around 1.57 g/cm³. The discrepancy in PETN single-crystal density results from ReaxFF equilibration at zero pressure and 300 K to eliminate residual stresses. The lower density reflects a tendency of this ReaxFF parametrization to somewhat overpredict the pressure at low compression. The Marsh data contain a series of unreacted shock data with shock velocities ranging from 2.760 to 5.385 km/s. The Dick data are obtained from unreacted shock of [110] and [001] PETN crystals, respectively. MSST shock simulations along [110], [001], and [100] orientations were performed with steady-state shock velocities ranging from 3 to 10 km/s, and the particle velocities were acquired at the moment when the system yields. Assuming a linear relationship between the shock velocities and the particle velocities, $U_s = C_0 + sU_p$, the intercepts C_0 , or the bulk sound velocities, and the slopes s are compared in Table 2. It is seen that C_0 and s compare reasonably well to experimental values, indicating the Hugoniot relations from MSST simulations with ReaxFF are in good agreement with experiments.

3.4. Temperature, Pressure, and Shear Stress Profiles. Temperature and pressure profiles for all MSST simulations along [110], [001], and [100] orientations with steady-state shock velocities ranging from 5 to 10 km/s are plotted in Figures 4 and 5, respectively. Intuitively, stronger shocks result in higher system temperatures and pressures. For the same shock velocities, the temperature differences between the shocks along the three different orientations are found to be within 150 K, which is relatively small so that the effect of temperature difference along different directions should be negligible. Plotted in Figure 6 are the system temperature and shear stress for the 10 km/s shock along the [110] orientation

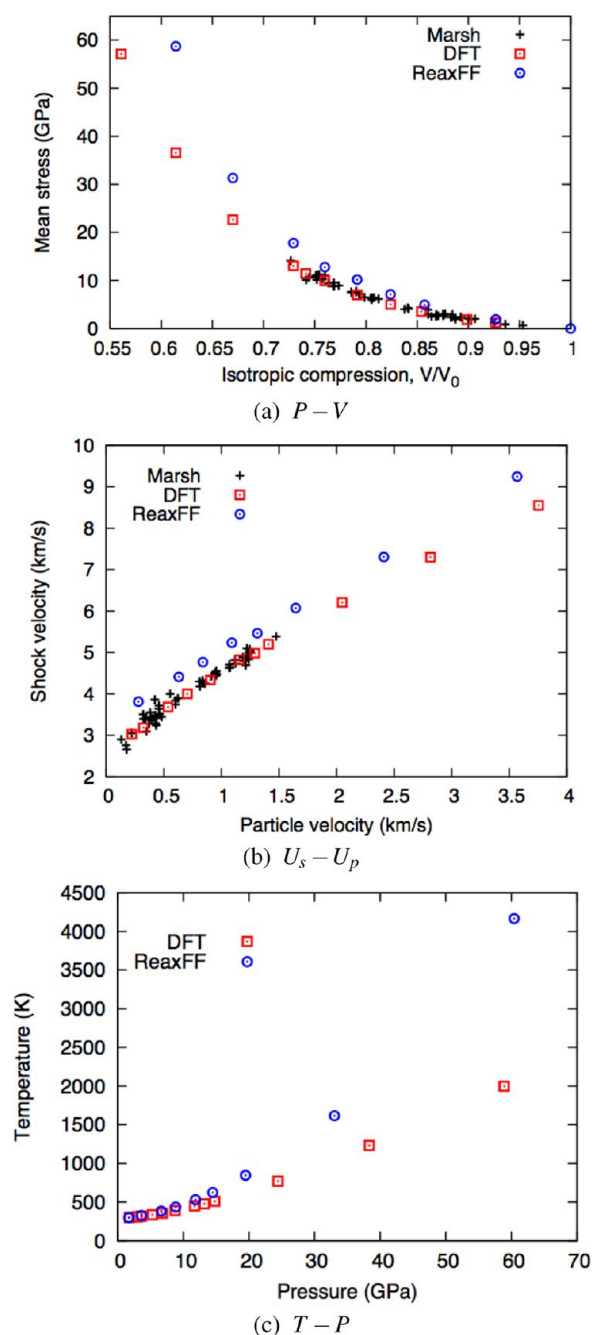


Figure 2. Bulk unreacted (a) mean stress–volume, (b) shock velocity–particle velocity, and (c) temperature–pressure Hugoniot plots of PETN single crystals via isotropic compressions, indicating ReaxFF MD predicts Hugoniot reasonably well compared to experiments and DFT MD calculations. Black crosses are experimental data from Marsh,³¹ red squares are our DFT MD calculations, and blue circles are our ReaxFF calculations.

from 0 to 2 ps, while illustrated in Figure 7 is the chemical species analysis of the system. In Figure 6, temperature of the system starts at 300 K and shear stress oscillates about 0 GPa. When the system contracts in response to the shock wave at 0.12 ps, shear stress experiences an abrupt rise to 50 GPa at 0.19 ps followed by another sharp drop to 5 GPa at 0.22 ps, indicating the yielding of the system due to the uniaxial compression. Meanwhile, temperature starts to rise at 0.14 ps, and reaches 3300 K at 0.21 ps. This stage of temperature rise is

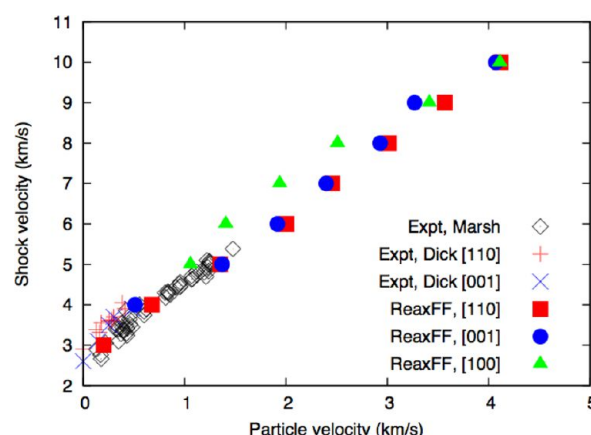


Figure 3. Shock velocity–particle velocity (U_s-U_p) Hugoniot plots of PETN single crystals along different shock orientations from experiments and ReaxFF calculations. Black diamonds are from Marsh data,³¹ cross symbols are from Dick's experiments,³ and closed symbols are our MSST simulations with ReaxFF via uniaxial compressions. Data indicate ReaxFF MD with MSST technique predicts U_s-U_p Hugoniot that agree well with experimental values.

Table 2. Intercepts and Slopes of U_s-U_p Relations

orientation	expt, Marsh ³¹		expt, Dick ³		this work	
	C_0	s	C_0	s	C_0	s
[110]	2.87	1.69	3.02	2.33	2.65	1.77
[001]			2.69	2.95	2.80	1.79
[100]			—	—	3.72	1.56

therefore due to a mixed elastic and plastic deformation of the system. During this first stage of temperature rise, no chemical reactions occur in the system. This is evident by examining Figure 7 from 0.0 to 0.2 ps, where only PETN molecules exist in the shocked system and no products are identified.

After the first mechanical deformation stage, the system temperature drops from 3300 to 3080 K between 0.20 and 0.23 ps, followed by a second stage rise that takes the temperature to 5600 K at 2 ps. The initial 220 K drop in temperature is due to the initiation of chemical reactions, which is presented in Figure 7, where the PETN concentration plummets to less than 0.1 times the original concentration from 0.19 to 0.21 ps, accompanied by a dramatic increase in NO_2 concentration in the system from 0.20 to 0.23 ps. Since the $\text{CO}-\text{NO}_2$ bond dissociation is an endothermic reaction, system temperature drops due to the conversion of kinetic energy to potential energy. As reaction initiates and primary products such as H_2O and OH (not shown in figure) are produced in the system, exothermic reactions are responsible for the rise of temperature from 3080 to 5600 K. In the last stage of energy release after 2 ps, the temperature rises to 6000 K, indicated by the red curve in Figure 4a. This is attributed to the formation of secondary products such as N_2 , NO , CO , and CO_2 (only N_2 is shown in Figure 7).

We can compare the axial stress in Figure 5c to the NEMD shock simulations of Budzien et al.⁵ In that work, a PETN crystal was driven against a stationary wall along its [100] orientation at a velocity (or particle velocity) of 4 km/s to generate a shock wave and chemical reactions. The speed at which the resultant shockwave propagated was 8.70 km/s, and the axial stress in the reacted system was approximately 52 GPa.⁵ From MSST simulations along the [100] orientation of

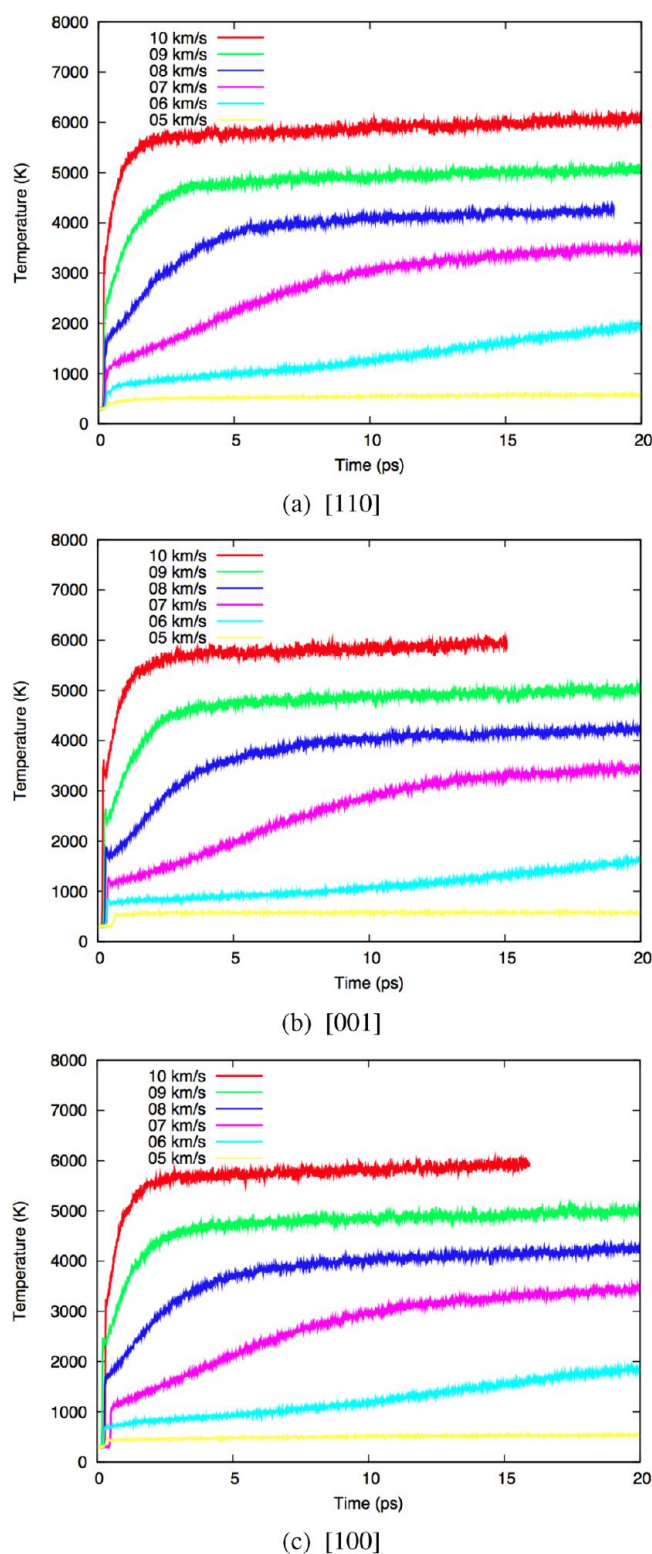


Figure 4. Temperature profiles for MSST shocks with ReaxFF along (a) [110], (b) [001], and (c) [100] orientations. Steady-state shock velocities indicated by the legend.

this work, axial stresses along the shock orientation are 78.3, 58.5, 42.7, 35.8, and 21.5 GPa for shock velocities of 10, 9, 8, 7, and 6 km/s (reacted systems). Linearly interpolating between the 8 and 9 km/s results gives an axial stress of 57 GPa at 8.70 km/s, in good agreement with the NEMD shock simulation.

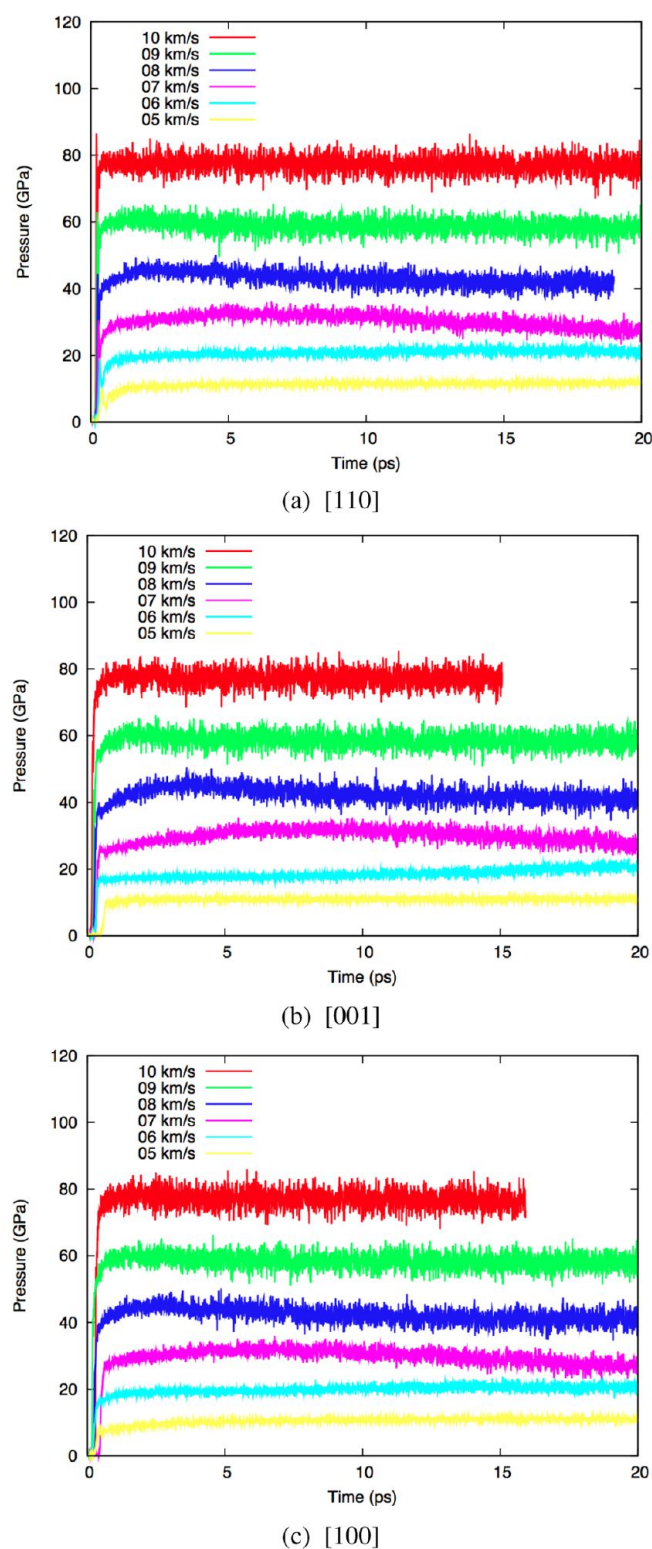


Figure 5. Pressure profiles for MSST shocks with ReaxFF along (a) [110], (b) [001], and (c) [100] orientations. Steady-state shock velocities indicated by the legend. The pressure profiles agree well with that obtained from a nonequilibrium molecular dynamics (NEMD) shock simulation.⁵

3.5. Orientational Shock Sensitivity. From MSST simulations, the lowest shock velocities that initiate reactions (as identified by the temperature profiles and chemical species analysis) for the [110], [001], and [100] orientations are $U_s =$

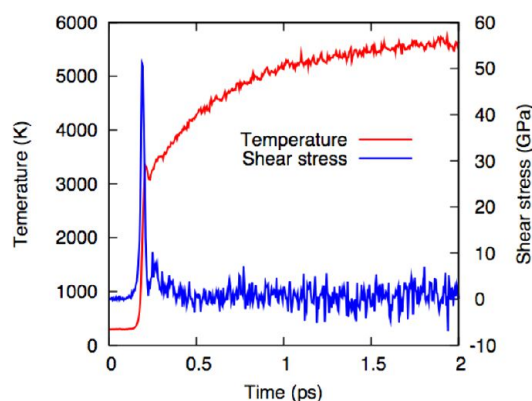


Figure 6. Temperature (red) and shear stress (blue) profiles during shock initiation for [110] shock with $U_s = 10$ km/s with ReaxFF using MSST. Rises in temperature indicate mechanical work and chemical reactions, while rise and drop in shear stress indicates the yielding of the structure.

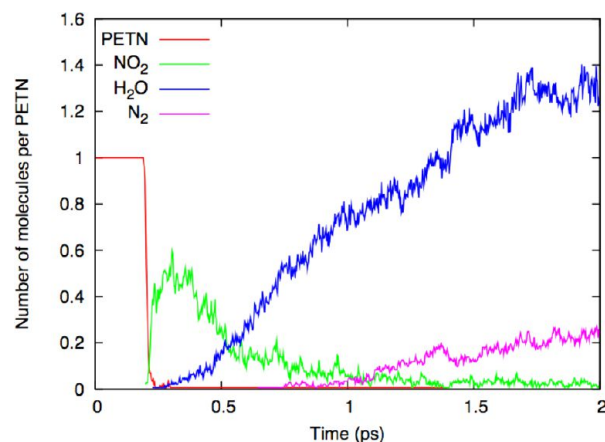


Figure 7. Major reactants and products during shock initiation for [110] shock with $U_s = 10$ km/s with ReaxFF using MSST. Red curve is PETN, green is NO_2 , blue is H_2O , and magenta is N_2 . Species concentrations are relative to the original number of PETN molecules. Chemical reactions initiate by the dissociation of PETN, forming NO_2 and H_2O , two primary products. Secondary products, such as N_2 , form latter.

5, 6, and 6 km/s, respectively. Using the conservation of momentum Rankine–Hugoniot relation, the shock initiation pressure can be estimated with the equation $P = \rho_0 U_s U_p$, where ρ_0 is the initial density (1.57 g/cm^3) of the PETN crystals. The steady-state particle velocities u_p are 1.621, 2.118, and 2.231 km/s for the [110], [001], and [100] orientations, respectively (see Table 3). The corresponding shock initiation stresses were calculated to be 12.7, 19.9, and 21.1 GPa, respectively. These shock initiation pressures agree qualitatively with the

Table 3. Comparison of Shock Initiation Stresses for Different Orientations from Experiments and Our Calculations

orientation	expt ³³	this work		
	stress (GPa)	stress (GPa)	U_s (km/s)	U_p (km/s)
[110]	8.40	12.7	5.0	1.621
[001]	13.3	19.9	6.0	2.118
[100]	31.3	21.1	6.0	2.231

experimentally measured values of 8.4–13.3 GPa for the [110] and [001] orientations, and 31.3 GPa for the [100] orientation.³³ The quantitative differences may be a consequence of the low initial density for the simulated PETN single crystals and also that shock simulations in this work are performed with supercells of about 4 nm in each direction. Nevertheless, this confirms that PETN is more sensitive along [110] and is less sensitive along [100], corresponding well to Dick's observation of orientation-dependent shock sensitivity.^{1–3}

3.6. Reaction Initiation Pathways. Illustrated in Figure 8 are concentration analyses of PETN and NO_x products, NO_2 , NO_3 , and NO , for shocks along the [110], [001], and [100]

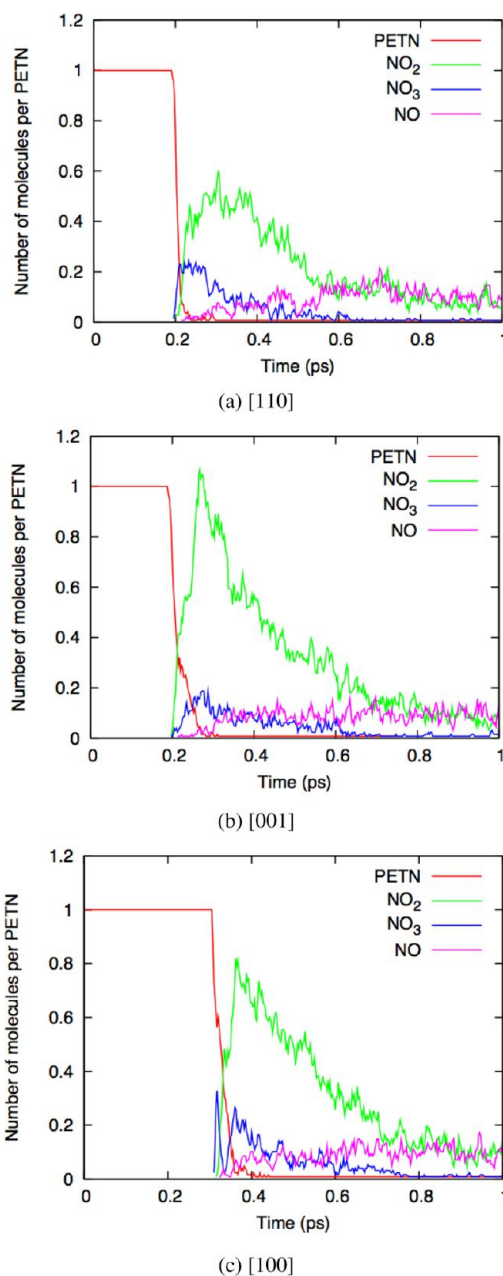


Figure 8. NO_x products formed for (a) [110], (b) [001], and (c) [100] shock with $U_s = 10$ km/s with ReaxFF using MSST, indicating differences in reaction initiation pathways: PETN (red), NO_2 (green), NO_3 (blue), and NO (magenta). [110] and [100] shocks initiate via mixed NO_2/NO_3 formation, while [001] is NO_2 dominant.

orientations with $U_s = 10$ km/s up to 1 ps. During the initial deformation stage, all systems are unreacted, as indicated by absence of species other than PETN until about 0.2–0.3 ps. As reaction initiates, PETN molecules start to decompose and NO_x products start to form. In all cases, the concentrations of NO_2 and NO_3 rise to maximum values before decreasing as they convert to secondary reaction products. The maximum concentration of NO_2 also exceeds that of NO_3 . However, in the case of [110] and [100] shocks, the formation of NO_3 precedes that of NO_2 , while for the [001] shock, the opposite is true. For the [100] shock, NO_3 forms first, but very quickly converts to NO_2 . The ratio of the maximum concentrations of NO_2 and NO_3 are 2.45, 5.89, and 2.53, for shock along [110], [001], and [100], respectively. This clearly indicates that the reaction initiation pathways are different for shock along different orientations. For [110] and [100] shocks, reaction initiates through mixed NO_2 and NO_3 formation, while NO_2 formation is dominant for [001] shocks.

Forming a nitrate group (NO_3) requires the breaking a C– ONO_2 bond, while forming a nitro group (NO_2) requires breaking a CO– NO_2 bond. In order to examine the effect of shock orientation on the roles played by the C– ONO_2 and CO– NO_2 bonds, Figure 9 shows the orientational distribution of CO– NO_2 (designated hereafter as O–N) and C– ONO_2 (designated as C–O) bonds relative to the [110], [001], and [100] crystal orientations. The distributions were obtained from configurations of the uncompressed crystal equilibrated at 300 K. A bond that is parallel to the shock orientation corresponds to 0° , and a bond that is perpendicular to the shock corresponds to 90° . Figure 10 shows the bonds in the PETN crystal with the shock directions lying horizontally on the page (left) and normal to the page (right).

For the [110] direction, the distributions of O–N and C–O bonds are bimodal and the bonds can be divided into two classes of equal size. Type I bonds are more aligned with the [110] direction, while type II bonds are more perpendicular. The type I C–O bonds are more aligned than the type I O–N bonds. In Figure 10, the type I C–O and O–N bonds are indicated with thick bonds. For [001] shock, Figures 9b and 10b, the orientational distributions are unimodal and the O–N bonds are more aligned than the C–O bonds. For the [100] direction, Figures 9c and 10c, the distributions are again bimodal. However, the degrees of alignment of the type I C–O and N–O bonds are not as distinct as in the case of the [110] direction.

Presented in Figure 11, a, b and c, are the vibrational kinetic energies, in units of kelvin, of the O–N and C–O bonds for [110], [001], and [100] shocks with $U_s = 10$ km/s up to 0.45 ps. System temperatures are also plotted for comparison. These bond kinetic energies are averaged over all the bonded atom pairs initially present in the system. Any pairs that subsequently dissociate are still included in the averaging. Center-of-mass momentum of the bonds is removed to exclude purely translational kinetic energy. The kinetic energy of a bond is taken to be the arithmetic average of the kinetic energies of the two atoms in the bond. The temperature of each atom i is calculated using the following equation:

$$\text{KE}_i = m_i(v_i - V_{\text{COM}})^2 / 3k_B$$

where m_i is the mass of the atom, v_i is the velocity of the atom, V_{COM} is the center-of-mass velocity of the bond, and k_B is the Boltzmann constant.

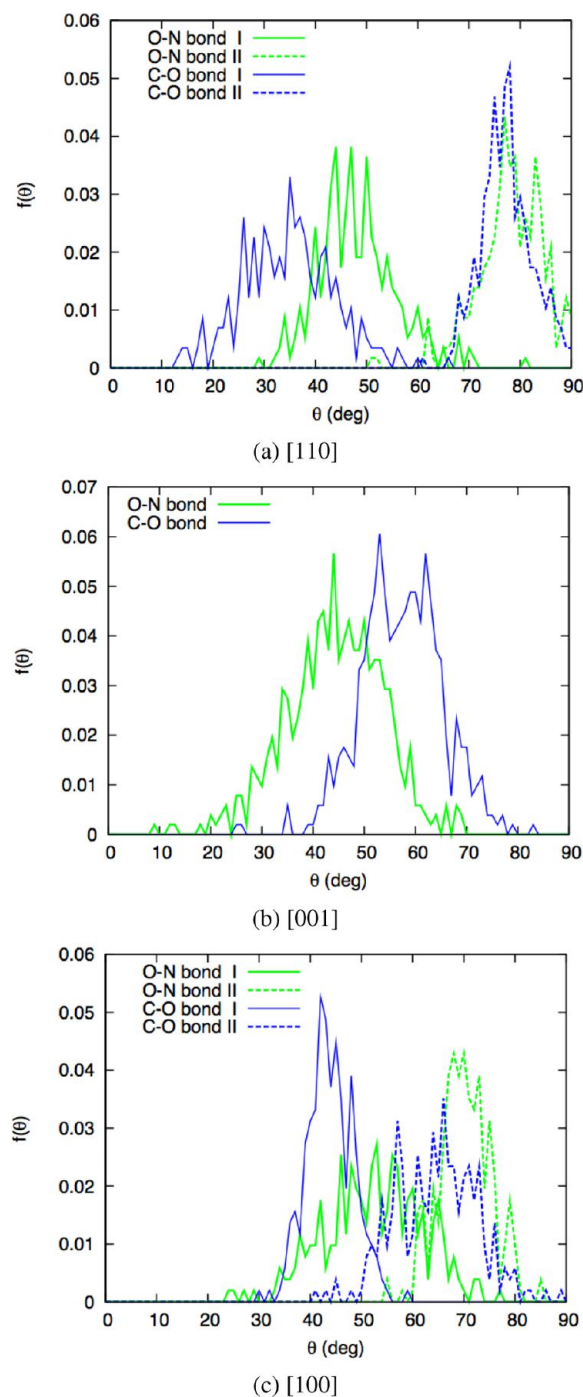


Figure 9. Orientational distribution function, $f(\theta)$, of CO– NO_2 (green) and C– ONO_2 (blue) bonds with respect to the shock orientation for (a) [110], (b) [001], and (c) [100] shock. For [110] and [100] shocks, type I C–O and O–N bonds, which are aligned more parallel with respect to the shock orientation, are solid lines, and type II C–O and O–N bonds, which are aligned more perpendicular with respect to the shock orientation, are dashed.

Bond kinetic energies on average oscillate about the system temperature. However, rises in bond kinetic energy can be interpreted as the conversion of potential energy to vibrational energy, while drops in bond kinetic energy indicate the opposite. For [110] shock, Figure 11a, type I C–O bonds that are more aligned with the shock direction acquire more kinetic energy (approximately 1800 K hotter) than type II C–O bonds

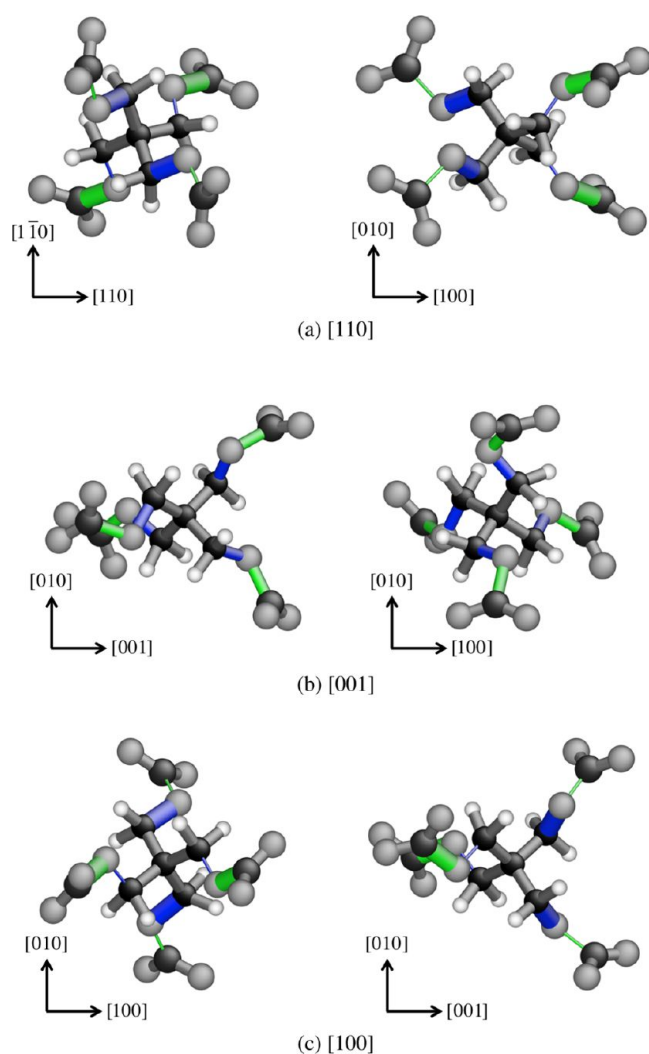


Figure 10. Visualization of bond alignment in the PETN crystal relative to (a) [110], (b) [001], and (c) [100] shock directions. In the left column, each image is rotated so that the shock direction is horizontal. In the right column, the shock direction is normal to the page. C-ONO₂ bonds are blue, and CO-NO₂ bonds are green. For [110] and [100] shocks, type I C-O and O-N bonds are thicker and type II C-O and O-N bonds are thinner.

and both types of O-N bonds at around 0.2 ps. This rise in kinetic energy of type I C-O bonds facilitates the dissociation of C-O bonds and the formation of nitrate groups. Note that, although type I C-O bonds are more thermally excited, still more nitro groups form due to a smaller dissociation barrier for the O-N bonds (refer to Table 1). The overall result is a large reduction in the NO₂/NO₃ ratio. Examining the bond temperatures for the [001] shock, as shown in Figure 11b, we observe an opposite trend. At 0.2 ps the O-N bonds are more thermally excited than the C-O bonds, approximately 600 K hotter, since O-N bonds are aligned more parallel to the shock orientation compared to the C-O bonds. Combined with a smaller dissociation barrier for O-N bonds, the NO₂/NO₃ ratio is significantly higher than that for [110] shocks. For [100] shock, Figure 11c, no significant differences in bond temperatures can be observed for both types of O-N and C-O bonds, which can be attributed to less distinct bond alignments compared to the two other orientations.:

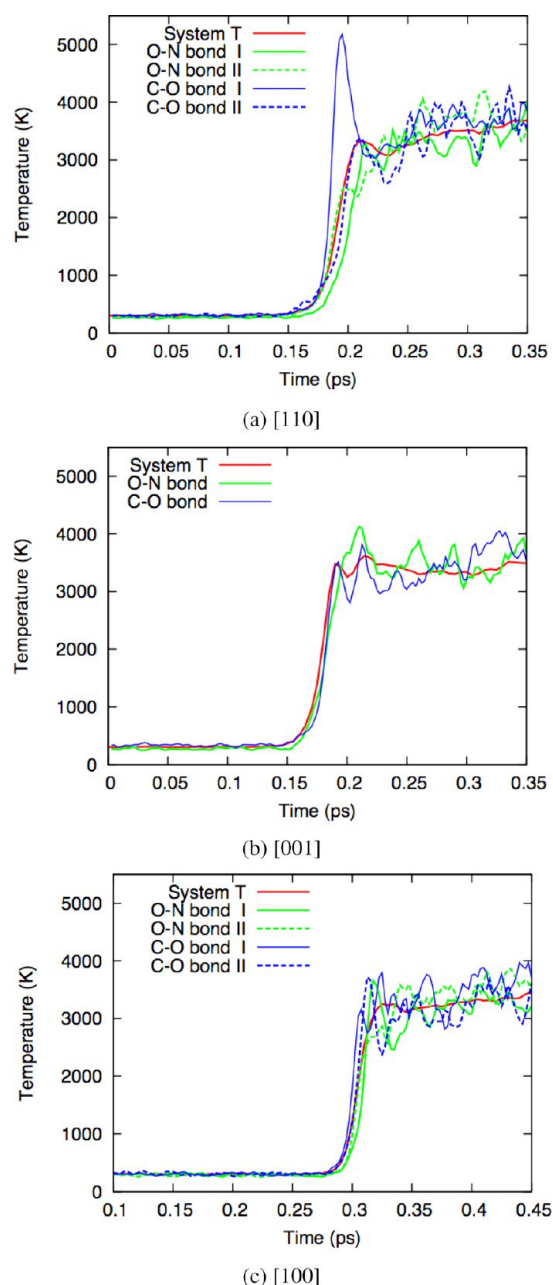


Figure 11. System temperatures (red) and averaged CO-NO₂ (green) and C-ONO₂ (blue) bond temperatures for (a) [110], (b) [001], and (c) [100] shock with ReaxFF using MSST. For [110] and [100] shocks, type I C-O and O-N bonds are solid lines and type II C-O and O-N bonds are dashed. Type I bonds, in particular for [110] shock, acquire more kinetic energy due to their alignments with respect to the shock orientation.

4. CONCLUSIONS

We investigated the dependence of reaction initiation mechanism in pentaerythritol tetranitrate (PETN) on shock orientation and shock strength with MD simulations using the ReaxFF potential and the MSST methodology. The ability of the ReaxFF potential to describe PETN was verified by qualitatively reproducing dissociation barriers of gas-phase PETN molecules from ab initio calculation.⁶ We also obtained reasonable pressure–volume, shock velocity–particle velocity, and temperature–pressure Hugoniot curves obtained from ReaxFF-MD simulations via isotropic compressions, when

compared to our DFT-MD simulations and established experimental data.^{31,32} Comparisons of the relationship between shock velocity and particle velocity from ReaxFF MSST shock simulations are also in good agreement with experimental data.^{3,31}

We found that, during shock initiation, the temperature of the shocked systems rises in three distinct stages, corresponding to mixed elastic and plastic deformation, primary chemical reactions, and secondary chemical reactions, respectively. From MSST shock simulations, the threshold shock velocities to initiate chemical reactions for the [110], [001], and [100] orientations are 5, 6, and 6 km/s. We found that shock initiation pressure is lowest for [110] and highest for [100], agreeing well with the notion that [110] is the most sensitive direction and [100] is the least. By analyzing the chemical species with on-the-fly time-averaged bond order information, we developed a more accurate methodology to analyze chemical species and identify chemical reactions. We found that NO₃ and NO₂ formation are the initial reaction products for all shocks considered in this work. However, mixed NO₃/NO₂ formation is observed for [110] shock while NO₂ formation is dominant for [001] shocks. For shock initiation along [110], C–ONO₂ bonds are aligned parallel to the shock orientation and hence acquire more kinetic energy than CO–NO₂ bonds, resulting in a larger amount of NO₃ formation. In contrast to this, for shock along [001], CO–NO₂ bonds are aligned parallel to the shock orientation and are therefore more thermally excited than the C–ONO₂ bonds. Together with a smaller dissociation barrier, NO₂ formation is the dominant reaction initiation mechanism for [001] shock.

AUTHOR INFORMATION

Corresponding Author

*E-mail: tnshan@sandia.gov.

Notes

The authors declare no competing financial interest.

ACKNOWLEDGMENTS

We acknowledge helpful discussions with Thomas R. Mattsson of Sandia National Laboratories. We acknowledge funding support from Department of Energy's Advanced Simulation and Computing and Sandia National Laboratories' Laboratory Directed Research and Development. Sandia National Laboratories is a multiprogram laboratory operated by Sandia Corp., a wholly owned subsidiary of Lockheed Martin Corp., for the US Department of Energy's National Nuclear Security Administration under contract DE-AC04-94AL85000.

REFERENCES

- (1) Dick, J.; Mulford, R.; Spencer, W.; Pettit, D.; Garcia, E.; Shaw, D. *J. Appl. Phys.* **1991**, *70*, 3572–3587.
- (2) Dick, J. *J. Appl. Phys. Lett.* **1992**, *60*, 2494–2495.
- (3) Dick, J. *J. Appl. Phys.* **1997**, *81*, 601–612.
- (4) Zybin, S. V.; Goddard, I.; William, A.; Xu, P.; van Duin, A. C. T.; Thompson, A. P. *J. Phys. Chem. B* **2010**, *114*, 8191.
- (5) Budzien, J.; Thompson, A. P.; Zybin, S. V. *J. Phys. Chem. B* **2009**, *113*, 13142–13151.
- (6) Wu, C.; Ree, F.; Yoo, C. *Propellants, Explos., Pyrotech.* **2004**, *29*, 296–303.
- (7) Dreger, Z. A.; Gruzdkov, Y. A.; Gupta, Y. M.; Dick, J. J. *J. Phys. Chem. B* **2002**, *106*, 247–256.
- (8) Wixom, R.; Mattsson, A.; Mattsson, T. Proceedings for 10th International GTPS Seminar and the 37th International Pyrotechnics Seminar in Reims 2011, France.
- (9) Knudson, M. D.; Desjarlais, M. P. *Phys. Rev. Lett.* **2009**, *103*, 225501.
- (10) Mattsson, T. R.; Lane, J. M. D.; Cochran, K. R.; Desjarlais, M. P.; Thompson, A. P.; Pierce, F.; Grest, G. S. *Phys. Rev. B* **2010**, *81*, 054103.
- (11) Armiento, R.; Mattsson, A. E. *Phys. Rev. B* **2005**, *72*, 085108.
- (12) Kresse, G.; Hafner, J. *Phys. Rev. B* **1993**, *47*, 558–561.
- (13) Kresse, G.; Hafner, J. *Phys. Rev. B* **1994**, *49*, 14251–14269.
- (14) Kresse, G.; Furthmüller, J. *Phys. Rev. B* **1996**, *54*, 11169–11186.
- (15) Mattsson, A. E.; Schultz, P. A.; Desjarlais, M. P.; Mattsson, T. R.; Leung, K. *Modell. Simul. Mater. Sci. Eng.* **2005**, *13*, R1–R31.
- (16) Conant, J. W.; Cady, H. H.; Ryan, R. R.; Yarnell, J. L.; Newsam, J. M. Technical Report LA-7756-MS, Los Alamos Scientific Laboratory, 1979.
- (17) van Duin, A.; Dasgupta, S.; Lorant, F.; Goddard, W. J. *J. Phys. Chem. A* **2001**, *105*, 9396–9409.
- (18) Chenoweth, K.; van Duin, A. C. T.; Goddard, I.; William, A. J. *J. Phys. Chem. A* **2008**, *112*, 1040–1053.
- (19) Strachan, A.; van Duin, A.; Chakraborty, D.; Dasgupta, S.; Goddard, W. *Phys. Rev. Lett.* **2003**, *91*, 098301.
- (20) Strachan, A.; Kober, E.; van Duin, A.; Ongaard, J.; Goddard, W. *J. Chem. Phys.* **2005**, *122*, 054502.
- (21) Reed, E.; Fried, L.; Joannopoulos, J. *Phys. Rev. Lett.* **2003**, *90*, 235503.
- (22) Manaa, M.; Reed, E.; Fried, L.; Galli, G.; Gygi, F. *J. Chem. Phys.* **2004**, *120*, 10146–10153.
- (23) Reed, E. J.; Manaa, M. R.; Fried, L. E.; Glaesemann, K. R.; Joannopoulos, J. D. *Nat. Phys.* **2008**, *4*, 72–76.
- (24) Mundy, C. J.; Curioni, A.; Goldman, N.; Kuo, I. F. W.; Reed, E. J.; Fried, L. E.; Ianuzzi, M. J. *J. Chem. Phys.* **2008**, *128*, 184701.
- (25) Manaa, M. R.; Reed, E. J.; Fried, L. E.; Goldman, N. *J. Am. Chem. Soc.* **2009**, *131*, 5483–5487.
- (26) Reed, E.; Maiti, A.; Fried, L. *Phys. Rev. E* **2010**, *81*, 016607.
- (27) Plimpton, S. J. *J. Comput. Phys.* **1995**, *117*, 1–19.
- (28) Aktulga, H. M.; Fogarty, J. C.; Pandit, S. A.; Grama, A. Y. *Parallel Comput.* **2012**, *38*, 245–259.
- (29) Henkelman, G.; Uberuaga, B.; Jonsson, H. *J. Phys. Chem.* **2000**, *113*, 9901–9904.
- (30) Henkelman, G.; Jonsson, H. *J. Phys. Chem.* **2000**, *113*, 9978–9985.
- (31) Marsh, S. P., Ed.; *LASL Shock Hugoniot Data*; Los Alamos Series on Dynamic Material Properties; University of California Press: Berkeley, CA, 1980.
- (32) Halleck, P.; Wackerle, J. *J. Appl. Phys.* **1976**, *47*, 976–982.
- (33) Yoo, C.; Holmes, N.; Souers, P.; Wu, C.; Ree, F.; Dick, J. *J. Appl. Phys.* **2000**, *88*, 70–75.